Supporting information for

Lattice-constant engineering of RuO_2 via Gd incorporation for for active and stable water splitting

*Ting Zhu[a, #], Shuming Ji[a, #], Xinlian Feng[a, #], Yuchi Wu[b], Zhongwei Yu[b], Xiaodong Pi[d], Shuhu Yin[a, *] and Jun Xu[a, c, *]*

[a]T. Zhu, S. Ji, X. Feng, S. Yin, Prof. J. Xu

[a] School of Microelectronics and School of Integrated Circuits (Jiangsu Key Laboratory of Semi. Dev. & IC Design, Package and Test), Nantong University, Nantong, 226019, P. R. China.

[b]Y. Wu, Z. Yu

[b] School of Physical Science and Technology, Nantong University, Nantong 226001, P. R. China.

[c] Prof. J. Xu

[c]National Laboratory of Solid State Microstructures, School of Electronics Science and Engineering, Collaborative Innovation Center of Advanced Microstructures, Jiangsu Provincial Key Laboratory of Advanced Photonic and Electrical Materials, Nanjing University, Nanjing, 210000, P. R. China.

[d]Prof. X. Pi

[d]State Key Laboratory of Silicon Materials, School of Materials Science and Engineering, Institute of Advanced Semiconductors, Hangzhou Innovation Center, Zhejiang University, Hangzhou, Zhejiang 310027, P. R. China.

[#]These authors contributed equally.

Email: shyin@ntu.edu.cn; junxu@nju.edu.cn.

Experimental

1.1 Chemicals

Ruthenium (III) chloride anhydrous ($RuCl_3$, ≥ 99.95%), Gadolinium (III) acetate hydrate ($Gd(CH_3CO_2)_3$, ≥ 99.9%) Hexamethylenetetramine (HMTA, ≥ 99%) were purchased from Aladdin-reagent Inc. Sulfuric acid (H_2SO_4, AR, ≥ 98%), ethylene glycol ($C_2H_6O_2$, EG, AR, ≥ 99.5%), ethanol (C_2H_6O, AR, ≥ 99.7%), isopropanol (C_3H_8O, AR, ≥ 99.7%) were purchased from Sinopharm Chemical Reagent Co. Ltd. (Shanghai, China). Vulcan XC-72 carbon black was purchased from Cabot. Commercial Pt/C (20 wt%) and commercial Ir/C (20 wt%) were purchased from Johnson Matthey (JM) Corporation. All the chemicals were used as received without further purification. The water (18 MΩ·cm) used in all experiments was prepared by passing through an ultra-pure purification system (Aqua Solutions).

1.2 Synthesis of $Gd_xRu_{1-x}O_2$ NPs

In a typical preparation of $Gd_{0.08}Ru_{0.92}O_2$ NPs, $RuCl_3$ (0.08 mmol), $Gd(CH_3CO_2)_3$ (0.008 mmol), HMTA (1.6 mmol), carbon powder (VXC-72, 32 mg) and H_2O (10 ml) were added into a vial (volume: 35 mL). After the vial had been capped, the mixture was ultrasonicated for around 15 min. The resulting homogeneous mixture was then heated at 80 °C for 1 h before it cooled down to room temperature. The products were collected by centrifugation and washed three times with acetone/ethanol mixture, and then calcined in a muffle furnace under 400 ºC in air for 2 h, to form the $Gd_{0.08}Ru_{0.92}O_2$ NPs.

The preparation of RuO_2 NPs, $Gd_{0.03}Ru_{0.97}O_2$ NPs, $Gd_{0.15}Ru_{0.85}O_2$ NPs, $Gd_{0.27}Ru_{0.73}O_2$ NPs and RuSe were similar to that of $Gd_{0.08}Ru_{0.92}O_2$ NPs except changing the amounts of $Gd(CH_3CO_2)_3$ from 0.008 mmol to 0 mmol, 0.004 mmol, 0.016 mmol and 0.032 mmol, respectively.

1.3 Characterization

The samples were prepared by dropping cyclohexane or ethanol dispersion of samples onto carbon-coated copper TEM grids using pipettes and dried under ambient condition. High-

resolution transmission electron microscopy (HRTEM) and scanning TEM (STEM) were conducted on an FEI Tecnai F20 transmission electron microscope at an accelerating voltage of 200 kV. Scanning electron microscopy (SEM) images and energy dispersive X-ray spectroscopy (EDS) were taken with a ZEISS Sigma field-emission scanning electron microscope operated at 15 kV. Powder X-ray Diffraction (PXRD) pattern was collected on Bruker D8 with a Cu Kα X-ray source (λ = 1.540598 Å). X-ray photoelectron spectra (XPS) was collected with an SSI S-Probe XPS Spectrometer. Fourier Transform Infrared Spectrometer (FTIR) was collected on PerkinElmer FT-IR Spectrometer Frontier.

1.4 Electrochemical measurements

For all the electrochemical tests, a three-electrode system was used to conduct the electrochemical measurements at an electrochemical workstation (CHI 760E). The catalyst (2.0 mg) was dispersed in 390 μL water-ethanol solution (3:1, v/v) and 10 μL 5 wt% Nafion by ultrasonicating for 1 h to form a homogeneous ink. The working electrode was fabricated by casting 10 μL catalyst ink onto a glassy carbon electrode (GCE) (diameter: 5 mm, area: 0.196 cm^2). The mass loading of the catalyst was 0.25 mg/cm^2. A graphite rod and a saturated calomel electrode (SCE) were used as counter electrode and the reference electrode, respectively. The reference was calibrated with respect to the reversible hydrogen electrode (RHE). Linear sweep voltammetry (LSV) was carried out at 5 mV s^{-1} at room temperature. For comparison, the commercial Pt/C and Ir/C were examined in all tests under the same conditions.

1.5 Electrochemical measurement of PEMWE

The anode catalyst ink ($Gd_{0.08}Ru_{0.92}O_2$ NPs) and cathode catalyst ink (commercial 20% Pt/C) were sprayed on N115 membrane. Then the N115 supported with catalysts were hot pressed under 10 MPa at 135 °C for 10 min. The load of cathode was 0.4 mg_{pt} cm^{-2} and the load of cathode was 0.3 mg_{Ru} cm^{-2} for $Gd_{0.08}Ru_{0.92}O_2$ NPs or 1.7 mg_{Ir} cm^{-2} for IrO_2. In order to construct a PEM device, porous titanium felt coated with Pt (200 μm) was used as the porous

transport layer (PTL) of anode, and carbon paper was used as the PTL of cathode. The active area was 1 cm^2.

The PEM device was operated at 80 ºC and the reactant was deionized water, which was circulated through a peristaltic pump. The polarization curve of the PEM was collected at the cell voltage of 1.2-2.0 V. The stability was tested by chronopotentiometry with a LANHE CT3002A at current densities of 0.1 A cm^{-2} at 60 ºC.

1.6 Computational details

All density function theory (DFT) computations were conducted adopting the Vienna Ab initio Simulation Package (VASP). The ion-electron interactions were depicted using the projector-augmented wave approach and the general gradient approximation in the Perdew-Burke-Ernzerhof (PBE) Form was applied. The convergence criteria were set to 0.05 eV $Å^{-1}$ and 10^{-4} eV for the residual force and energy during the structure relaxation, respectively. The plane-wave cutoff energy was set to be 500 eV. The 2 × 2 × 1 k-points were served as the samples in the Brillouin region. The Gibbs free energies of H* (ΔG_{H*}) was calculated using the formula of $\Delta G_{H*} = \Delta E_{H*} + \Delta E_{ZPE} - T\Delta S$. The vacuum thickness is set to the value larger than 15 Å in order to separate any two adjacent particles for lattice coupling.

1.7 Active Sites Calculations

The number of active sites (n) can be qualified based on the underpotential deposition (UPD) copper stripping charge (Q_{Cu}, $Cu_{UPD} \rightarrow Cu^{2+} + 2e^-$) with the following formula:

$n = Q_{Cu} / 2F$,

where F is the Faraday constant (C mol^{-1}).

1.8 Turnover Frequency (TOF) Calculations

TOF was calculated using the following formula:

$TOF = I / (2Fn)$,

where I is the current (A) during the linear sweep measurement, F is the Faraday constant (C mol^{-1}), n is the active sites (mol).[1]

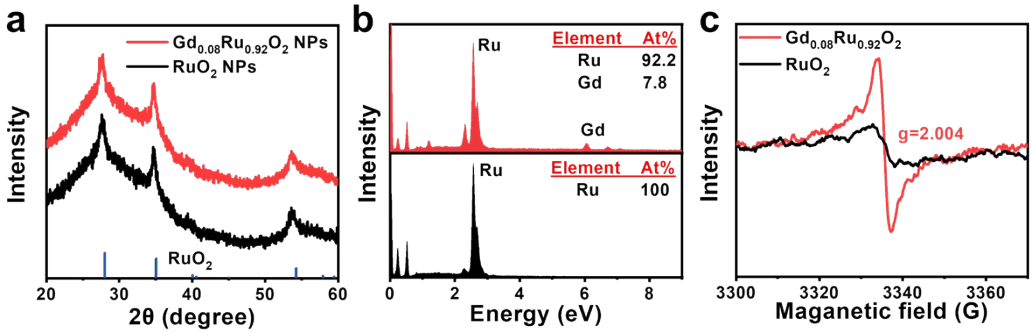

Fig. S1. (a) XRD patterns, (b) EDS patterns and (c) EPR spectra of $Gd_{0.08}Ru_{0.92}O_2$ NPs and RuO_2 NPs.

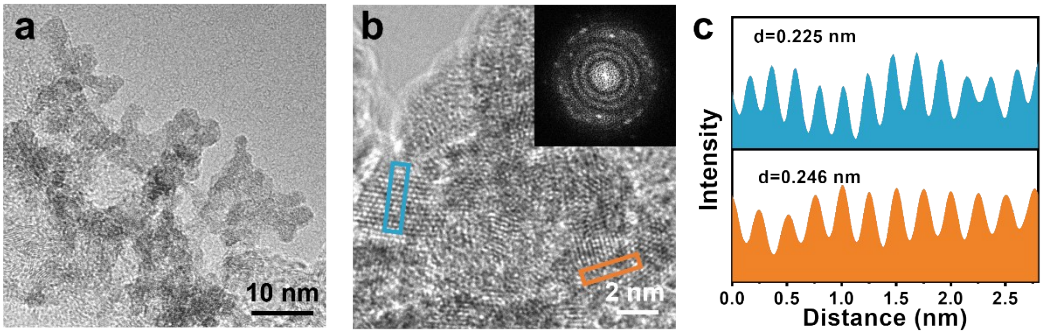

Fig. S2. (a, b) TEM image (inset: FFT pattern) and (c) corresponding intensity profile of RuO_2 NPs.

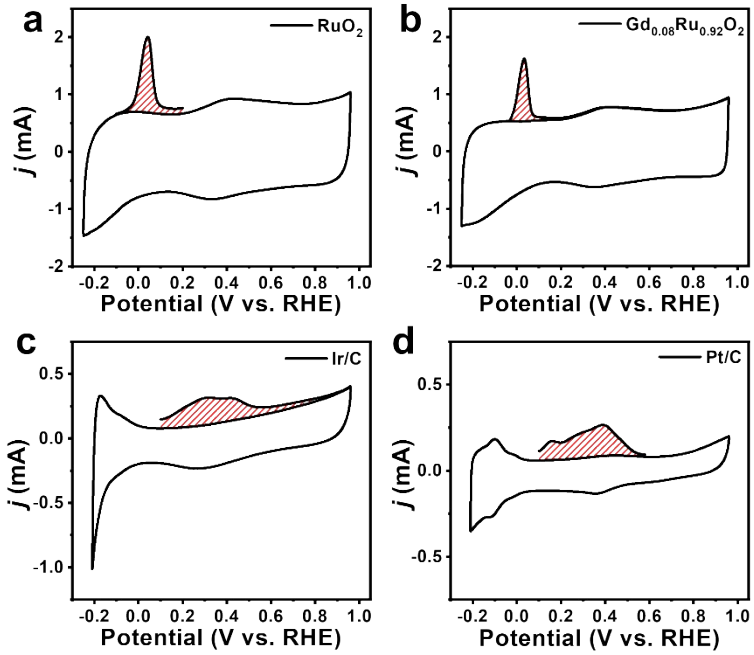

Fig. S3. Copper UPD in 0.5 M H_2SO_4 + 5 mM $CuSO_4$ on (a) RuO_2 NPs, (b) $Gd_{0.08}Ru_{0.92}O_2$ NPs and (c) Ir/C and (d) Pt/C. The electrodes were polarized at 0.26 V (vs. RHE) for 100 s to form the UPD layer.

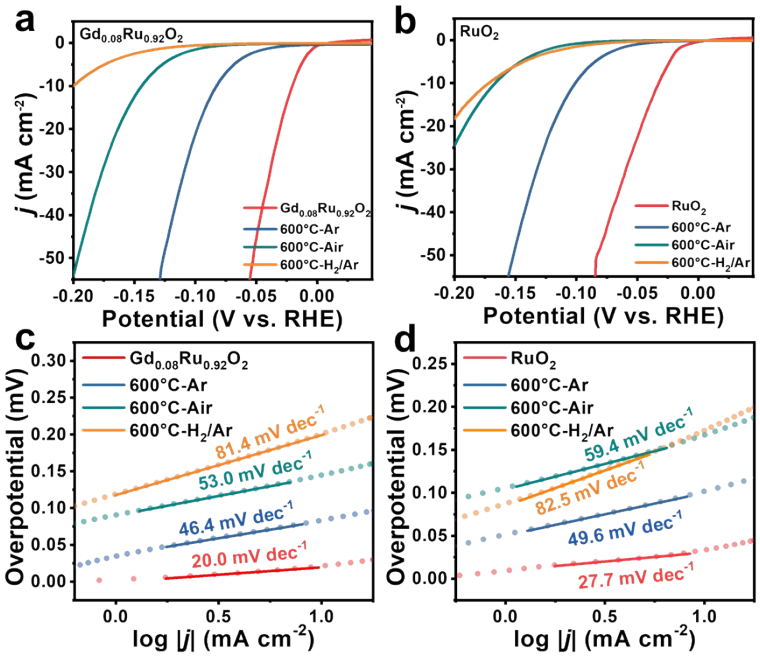

Fig. S4. (a) HER polarization curves, (b) Tafel slopes of $Gd_{0.08}Ru_{0.92}O_2$ NPs under different atmospheres. (c) HER polarization curves, (d) Tafel slopes of RuO_2 NPs under different atmospheres.

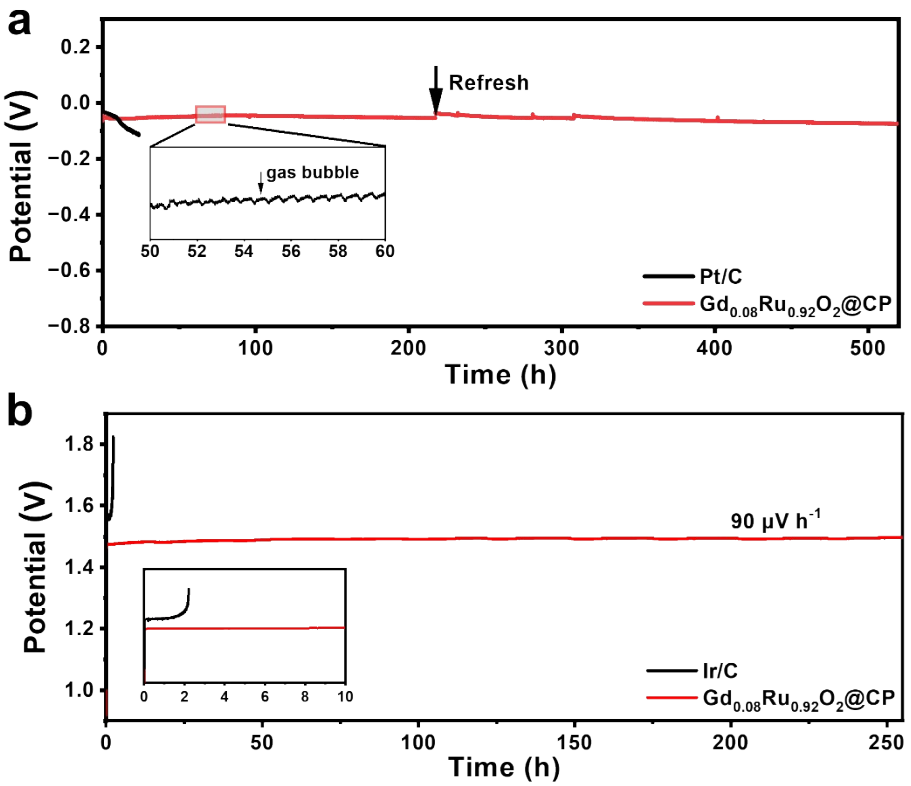

Fig. S5. (a) HER chronopotentiometry stability measurements at 10 mA cm^{-2} of $Gd_{0.08}Ru_{0.92}O_2$ NPs and Pt/C. (b) OER chronopotentiometry stability measurements at 10 mA cm^{-2} of $Gd_{0.08}Ru_{0.92}O_2$ NPs and Ir/C.

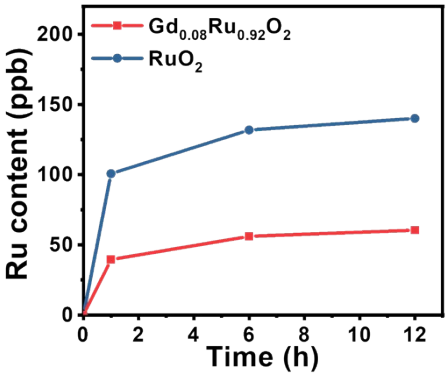

Fig. S6. Ru contents in the electrolyte of $Gd_{0.08}Ru_{0.92}O_2$ NPs and RuO_2 at 0.5 M H_2SO_4 during OER.

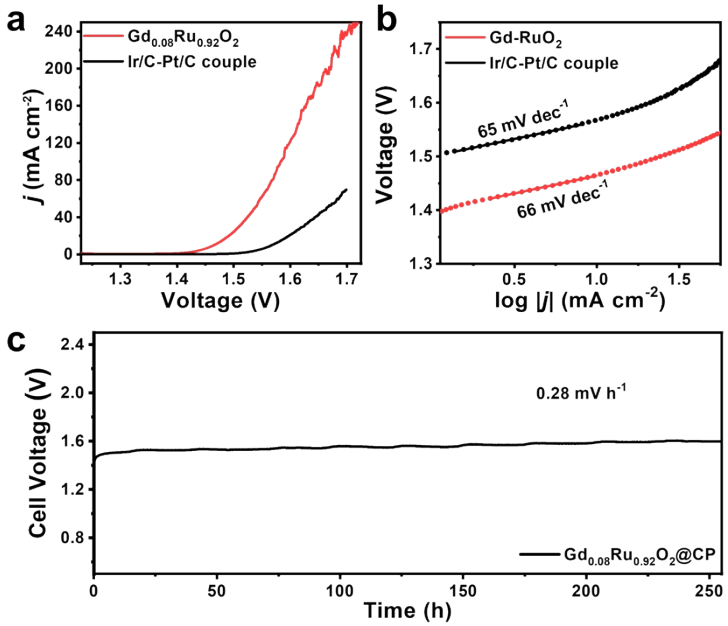

Fig. S7. (a) Overall water splitting performance and (b) Tafel slope of $Gd_{0.08}Ru_{0.92}O_2$ NPs and Ir/C-Pt/C couple, (c) chronopotentiometry stability measurements at 10 mA cm^{-2} of $Gd_{0.08}Ru_{0.92}O_2$ NPs.

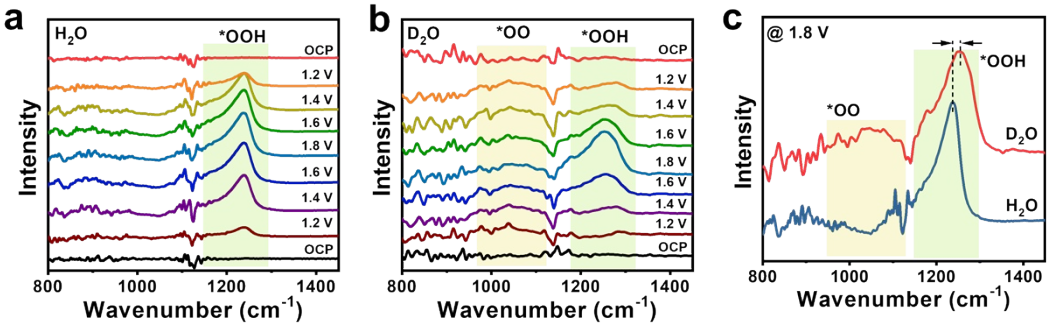

Fig. S8. In-situ ATR-SEIRAS at voltages from OCP to 1.8 V vs. Ag/AgCl for $Gd_{0.08}Ru_{0.92}O_2$ NPs in (a) H_2O and (b) D_2O. (c) Comparison of $Gd_{0.08}Ru_{0.92}O_2$ NPs at 1.8V vs. Ag/AgCl in H_2O and D_2O.

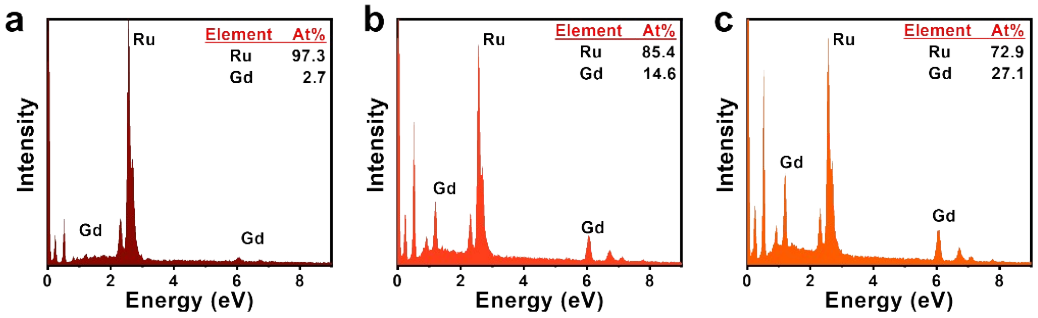

Fig. S9. EDS patterns of (a) $Gd_{0.03}Ru_{0.97}O_2$ NPs, (b) $Gd_{0.15}Ru_{0.85}O_2$ NPs and (c) $Gd_{0.27}Ru_{0.73}O_2$ NPs.

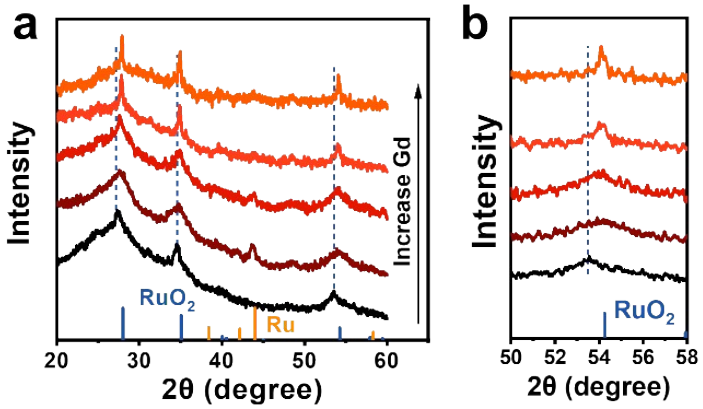

Fig. S10. (a, b) XRD patterns of RuO_2 NPs, $Gd_{0.03}Ru_{0.97}O_2$ NPs, $Gd_{0.08}Ru_{0.92}O_2$ NPs, $Gd_{0.15}Ru_{0.85}O_2$ NPs and $Gd_{0.27}Ru_{0.73}O_2$ NPs.

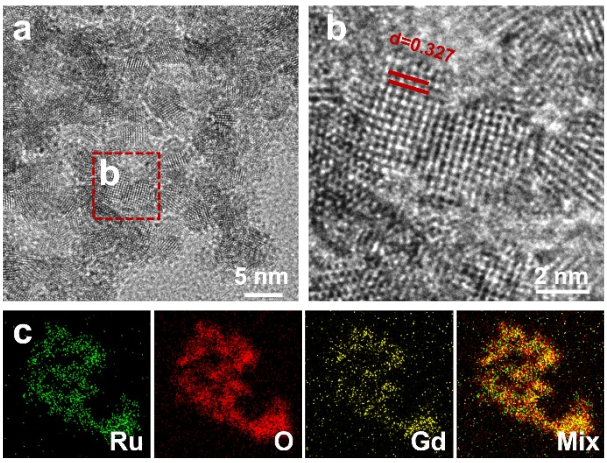

Fig. S11. (a, b) HRTEM images and (c) EDS element mapping images of $Gd_{0.27}Ru_{0.73}O_2$ NPs.

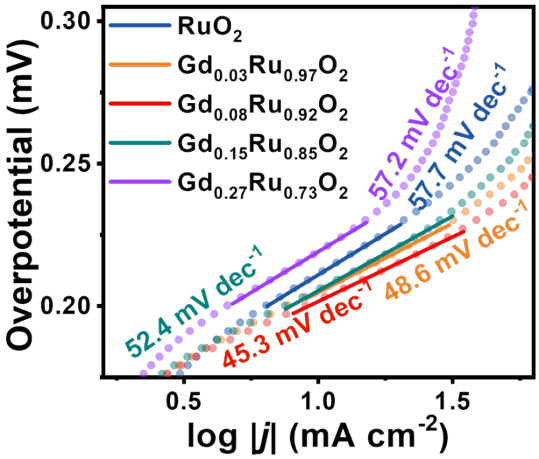

Fig. S12. Tafel slope of $Gd_xRu_{1-x}O_2$ NPs for OER in 0.5 M H_2SO_4.

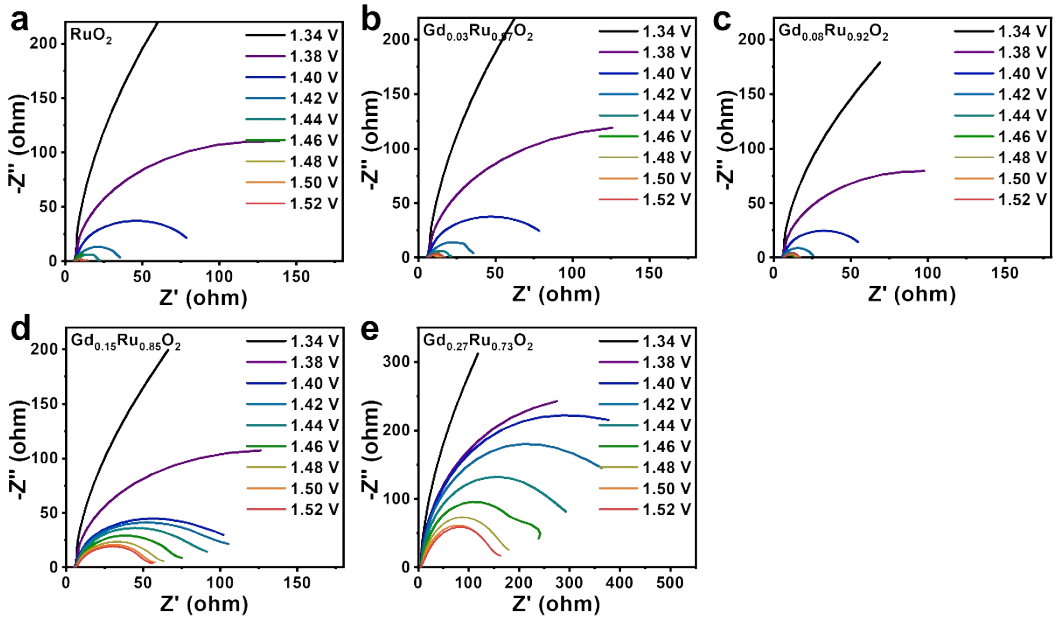

Fig. S13. EIS Nyquist plots (a) RuO_2 NPs, (b) $Gd_{0.03}Ru_{0.97}O_2$ NPs, (c) $Gd_{0.08}Ru_{0.92}O_2$ NPs, (d) $Gd_{0.15}Ru_{0.85}O_2$ NPs and (e) $Gd_{0.27}Ru_{0.73}O_2$ NPs under different potentials.

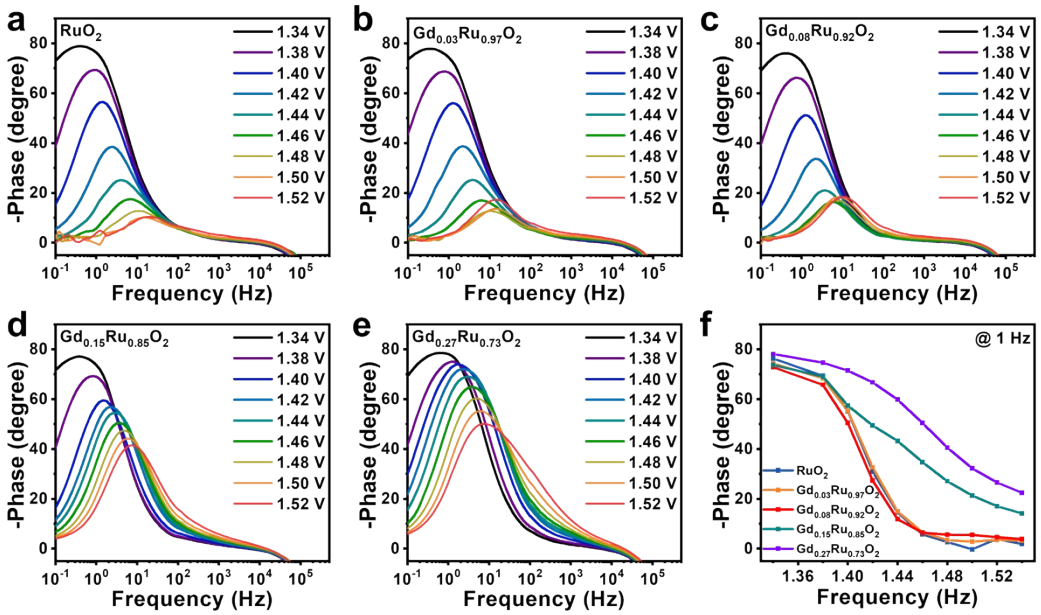

Fig. S14. Bode phase plots of (a) RuO_2 NPs, (b) $Gd_{0.03}Ru_{0.97}O_2$ NPs, (c) $Gd_{0.08}Ru_{0.92}O_2$ NPs, (d) $Gd_{0.15}Ru_{0.85}O_2$ NPs and (e) $Gd_{0.27}Ru_{0.73}O_2$ NPs under different potentials.

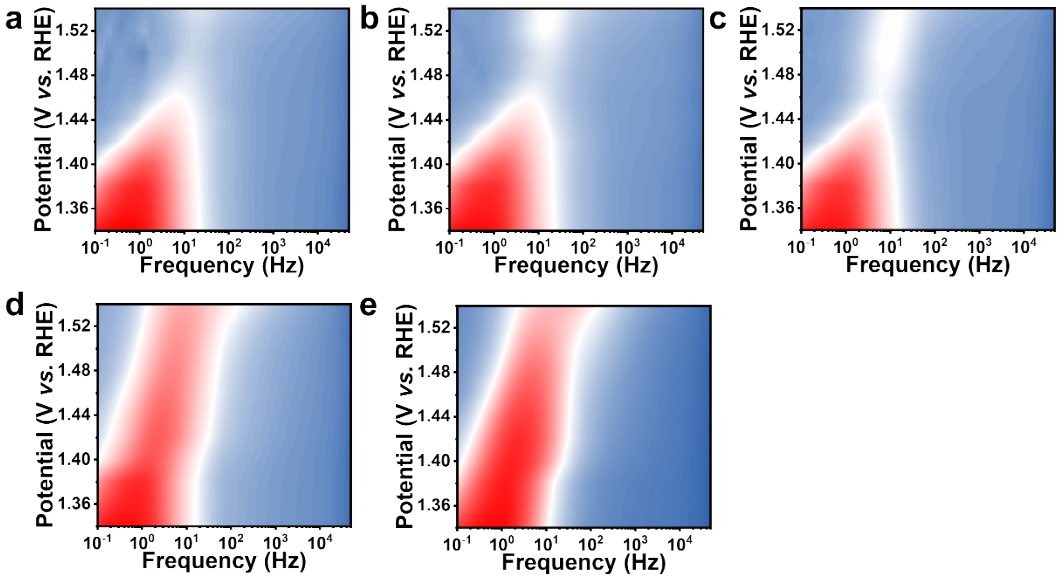

Fig. S15. Bode phase plots of (a) RuO_2 NPs, (b) $Gd_{0.03}Ru_{0.97}O_2$ NPs, (c) $Gd_{0.08}Ru_{0.92}O_2$ NPs, (d) $Gd_{0.15}Ru_{0.85}O_2$ NPs and (e) $Gd_{0.27}Ru_{0.73}O_2$ NPs under different potentials.

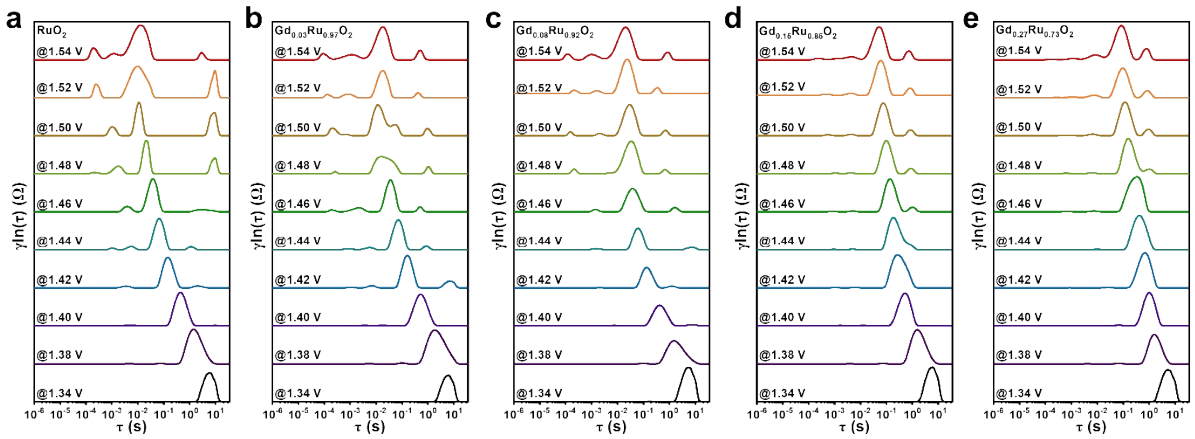

Fig. S16. EIS-DRT plots (a) RuO_2 NPs, (b) $Gd_{0.03}Ru_{0.97}O_2$ NPs, (c) $Gd_{0.08}Ru_{0.92}O_2$ NPs, (d) $Gd_{0.15}Ru_{0.85}O_2$ NPs and (e) $Gd_{0.27}Ru_{0.73}O_2$ NPs under different potentials.

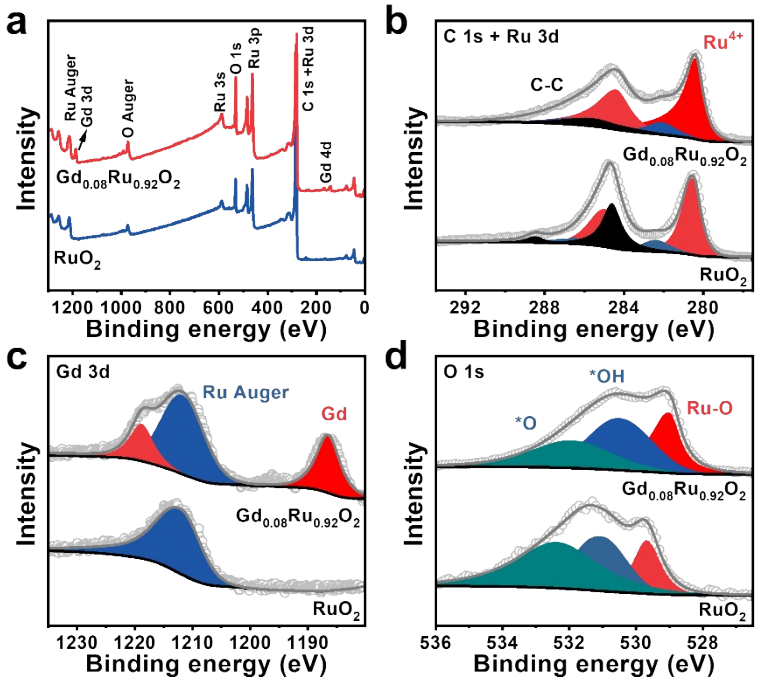

Fig. S17. (a) XPS spectra of (a) survey, (b) Ru 3d, (c) Gd 3d and (d) O 1s of RuO_2 and $Gd_{0.08}Ru_{0.92}O_2$.

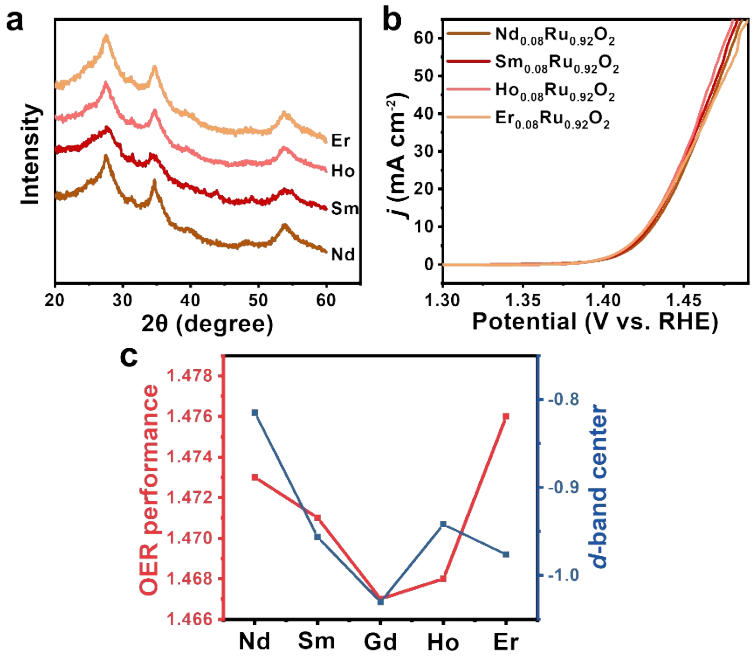

Fig. S18. (a) XRD patterns, (b) OER polarization curves and (c) overpotential at 50 mA cm^{-2} and d-band center of $Nd_{0.08}Ru_{0.92}O_2$, $Sm_{0.08}Ru_{0.92}O_2$, $Ho_{0.08}Ru_{0.92}O_2$, $Er_{0.08}Ru_{0.92}O_2$.

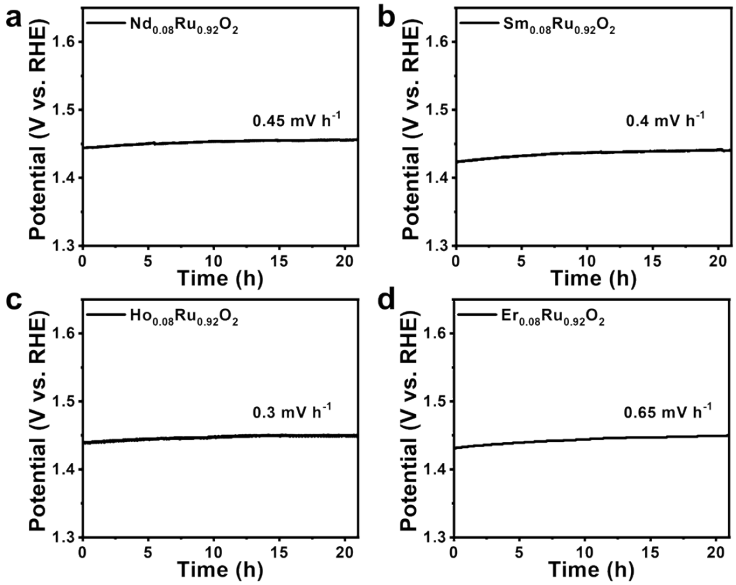

Fig. S19. OER chronopotentiometry stability measurements at 10 mA cm^{-2} of (a) $Nd_{0.08}Ru_{0.92}O_2$, (b) $Sm_{0.08}Ru_{0.92}O_2$, (c) $Ho_{0.08}Ru_{0.92}O_2$ and (d) $Er_{0.08}Ru_{0.92}O_2$.

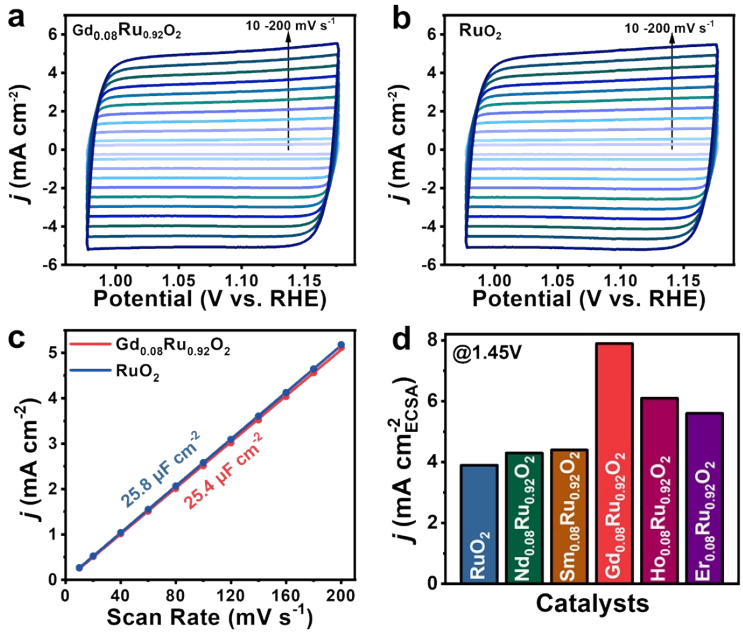

Fig. S20. Cyclic voltammetry curves of (a) $Gd_{0.08}Ru_{0.92}O_2$ and (b) RuO_2 collected at various scan rates from 10 to 200 mV s^{-1}, (c) The capacitive currents at the potential of 1.1 V (vs. RHE) as a function of scan rates. (d) Current densities normalized to the electrochemically active surface area at 1.45 V vs. RHE.

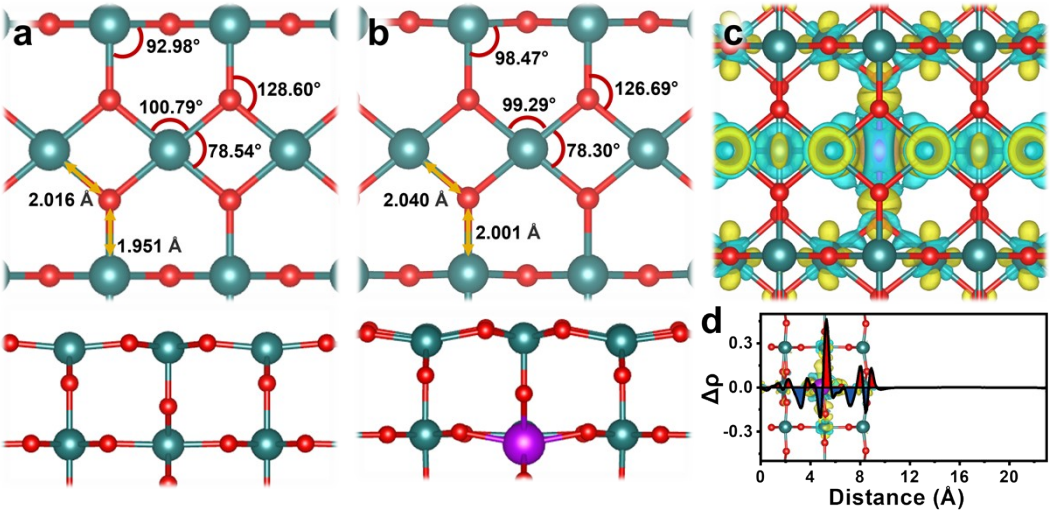

Fig. S21. Crystal structure of (a) RuO_2 and (b) $Gd_{0.08}Ru_{0.92}O_2$. (c, d) Charge density difference analysis of $Gd_{0.08}Ru_{0.92}O_2$.

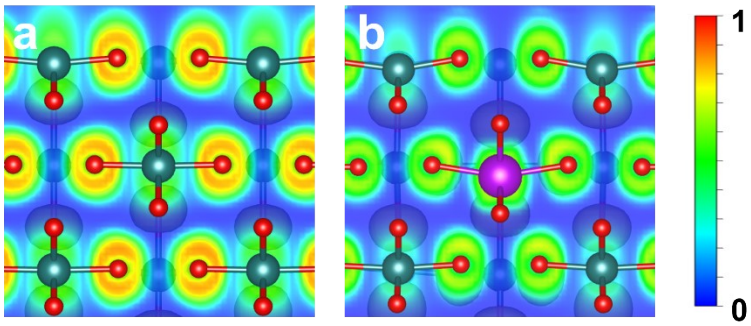

Fig. S22. Side view of ELF maps of (a) RuO_2 and (b) $Gd_{0.08}Ru_{0.92}O_2$.

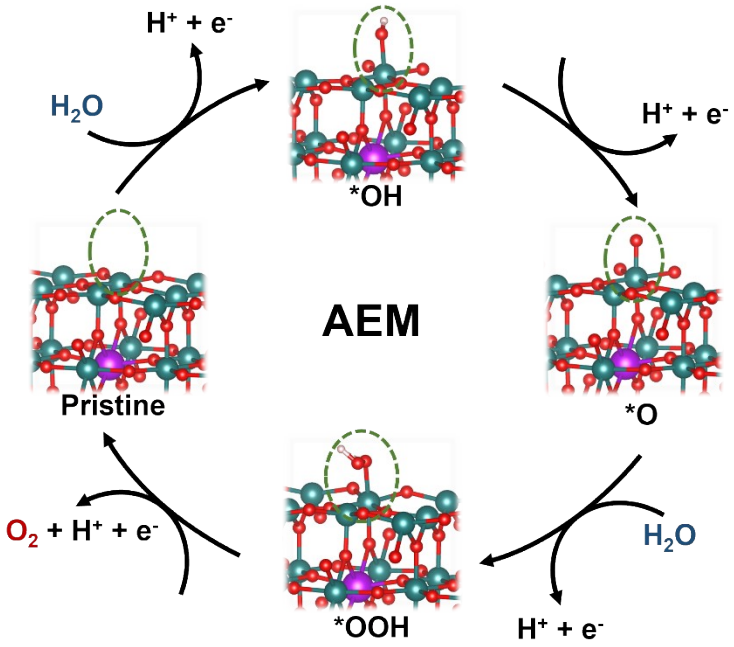

Fig. S23. The surface intermediates evolution process of AEM pathway for $Gd_{0.08}Ru_{0.92}O_2$.

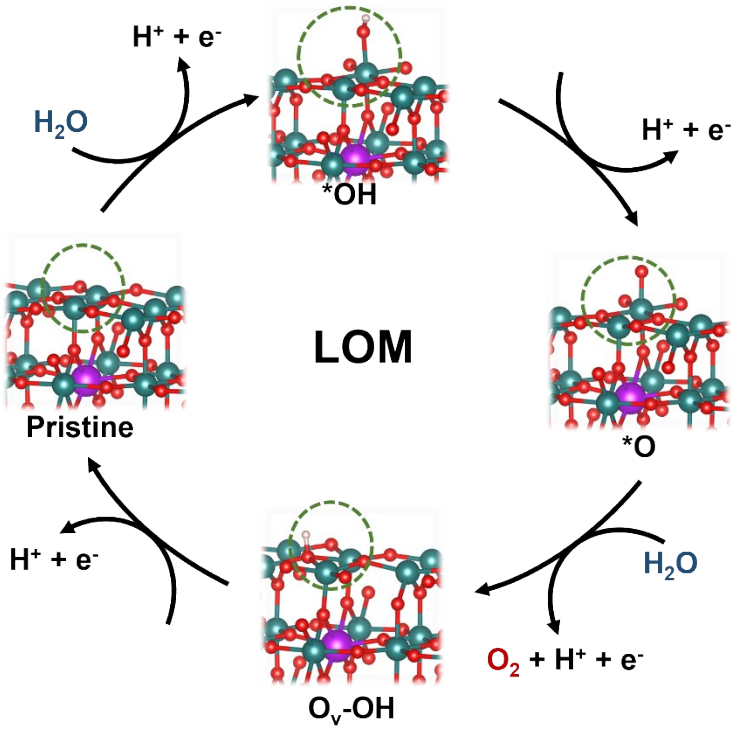

Fig. S24. The surface intermediates evolution process of LOM pathway for $Gd_{0.08}Ru_{0.92}O_2$.

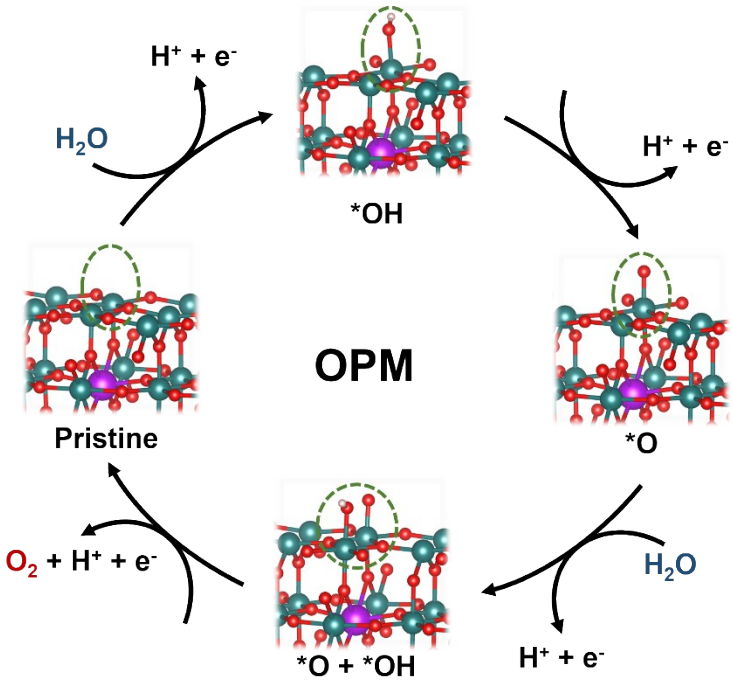

Fig. S25. The surface intermediates evolution process of OPM pathway for $Gd_{0.08}Ru_{0.92}O_2$.

Table S1. The comparison of the HER, OER, and overall water splitting performances of $Gd_{0.08}Ru_{0.92}O_2$ NPs and various reported Ru-based electrocatalysts (at 10 mA cm^{-2}).

Electrocatalyst	Electrolyte	HER (mV)	OER (mV)	Overall voltage (V)	Reference
$Gd_{0.08}Ru_{0.92}O_2$ NPs	**0.5 M H_2SO_4**	**18**	**202**	**1.465**	**This work**
SiO_x/$RuCoO_x$ NPs	0.5 M H_2SO_4	18	217	1.482	*Rare Met.* **2025**, *44*, 6223-6231.
Ru-VO_2	0.5 M H_2SO_4	46	228	1.515	*Adv. Mater.* **2024**, *36*, 2310690.
RuO_2/CeO_2	0.5 M H_2SO_4	120	170	1.54	*Chem. Eng. J.* **2024**, *479*, 147939.
Ru@RuO_2-250	0.5 M H_2SO_4	31	198	1.48	*Chem. Eng. J.* **2023**, *460*, 141672.
RuO_2/WC	0.5 M H_2SO_4	58	347	1.66	*Angew. Chem. Int. Ed.* **2022**, *61*, e202202519.
$Ni_{cluster}$-Ru NWs	0.5 M H_2SO_4	20	205	1.454	*Energy Environ. Sci.,* **2021**, *14*, 3194-3202
RuIr-NC	0.05 M H_2SO_4	46	165	1.485	*Nat. Commun.* **2021**, *12*, 1145.
a-$RuTe_2$	0.5 M H_2SO_4	33	245	1.52	*Nat. Commun.* **2019**, *10*, 5692
$RuIrO_x$	0.5 M H_2SO_4	12	233	1.45	*Nat. Commun.* **2019**, *10, 4875*
h-PNRO/C	0.1 M $HClO_4$	59.9	240	1.524	*Adv. Mater.* **2019**, *31,* e1805546
Co-RuIr	0.1 M $HClO_4$	13.8	235	1.52	*Adv. Mater.* **2019**, *31,* e1900510.
Ru_3Ni_3 NAs	0.5 M H_2SO_4	39	252	1.51	*iScience* **2019**, *11*, 492-504
Ru nanosheets	0.5 M H_2SO_4	20	220	1.53	*ACS Catal.* **2016**, *6*, 1487-1492.

1. a